ANALYZING THE INFLUENCE OF MORPHOLOGY AND CONNECTIVITY OF GRAIN BOUNDARIES ON THEIR VELOCITY DURING ABNORMAL GRAIN GROWTH IN AN ALUMINUM ALLOY

THOMAS WILHELM[1], HELMUTH-ANDRÉ SCHULZ-HARDER[3], ORKUN FURAT[1,2], JULES M. DAKE[3], CARL E. KRILL III[3], VOLKER SCHMIDT[1]

[1]*Institute of Stochastics, Ulm University, 89069 Ulm, Germany*
[2]*SDU Applied AI and Data Science Unit, University of Southern Denmark, Campusvej 55, 5230 Odense, Denmark*
[3]*Institute of Functional Nanosystems, Ulm University, 89081 Ulm, Germany*

Abstract. Grain growth in polycrystalline materials has conventionally been described by curvature-driven models, which assume a direct proportionality between grain boundary (GB) velocity and mean curvature. However, recent experimental and computational studies have revealed significant deviations of GB migration from conventional models. These discrepancies become particularly pronounced during abnormal grain growth (AGG), where a small fraction of grains exhibits disproportionately rapid growth that cannot be fully explained by existing theoretical models. This study extends previous experimental studies of AGG in a commercial Al-Mg alloy (AA5252) by representing GBs obtained from time-resolved, synchrotron-based diffraction-contrast tomography (DCT) measurements by continuous surfaces, overcoming the limitations associated with voxel-based microstructural data. Such surface representations facilitate the analysis of the relationship between pointwise (local) mean curvatures and GB velocities, while additionally accounting for potential pinning effects arising from second-phase particles measured by phase-contrast tomography (PCT). By linking these localized GB dynamics with the connectivity of GBs, the findings provide insight into microstructural evolution during AGG.

Keywords: polycrystalline material; kinetics of grain growth; abnormal grain growth; spherical harmonics representation; 3D microstructure mapping; 3DXRD microscopy

1. Introduction

For more than a century, grain growth in polycrystalline materials—composed of numerous individual crystallites (grains) having distinct crystallographic orientations separated by grain boundaries (GBs)—has attracted significant research interest due to the strong influence of grain size on the resulting materials properties. Early investigations established that curved GBs migrate toward their center of curvature [1], and Burke and Turnbull's analytic model [2]—later extended by Hillert [3]—explained the parabolic relationship between the average grain size and the annealing time during normal grain growth, under the assumption that the velocity v of a GB is given by $v = M\gamma\overline{H}$, with mobility M, excess energy per unit area γ and mean curvature $\overline{H}$.

However, significant discrepancies persist between the predictions of this model and experimental observations. Advancements in high-resolution characterization techniques—such as

orientational imaging microscopy [4], automated serial sectioning [5, 6], and X-ray diffraction-based microscopy [7]—have revealed complexities in grain size distributions and microstructural evolution that current analytic models fail to capture [8]. Crucially, recent experimental measurements and numerical simulations indicate that, in certain materials systems, GB velocity is not correlated with GB mean curvature [9–12]. It has even been proposed that grain growth fundamentally cannot be characterized as the result of curvature-driven GB migration [13]. In particular, reported instances of GBs moving away from their center of curvature—referred to as anticurvature migration—are not compatible with current curvature-driven grain growth models [14, 15].

These theoretical limitations become particularly pronounced during abnormal grain growth (AGG), a phenomenon in which a minority fraction of grains grows rapidly in comparison to the surrounding grains. Current models adequately capture neither the physical emergence of the so-called *abnormal* grains nor the persistence of their kinetic advantage. While the exact thermodynamic mechanisms underlying AGG remain incompletely resolved [16], the literature predominantly identifies two possible drivers. First, due to the presence of crystallographic texture, AGG can initiate when a small fraction of grains deviates from the dominant crystallographic texture of the polycrystal [17–19]. Consequently, the GBs of such grains exhibit high misorientation angles. According to conventional theory, these highly misoriented boundaries possess greater specific energies [20] and mobilities [21] compared to low-angle boundaries and, thus, migrate faster than other GBs. Secondly, when a sample contains second-phase particles, the latter can promote AGG by selectively retarding or arresting the migration of specific GBs through Zener pinning [22–24].

To bridge the gap between empirical observation and predictive modeling, recent efforts have introduced a reverse engineering approach, which extracts the governing model parameter values directly from experimentally acquired three-dimensional (3D) datasets of evolving GB networks [25]. This methodology requires the nondestructive, time-resolved 3D mapping of polycrystalline microstructures under isothermal annealing conditions. Applying this approach, a recent study [26] utilized diffraction-contrast tomography (DCT) [27, 28] to map AGG in the commercial aluminum alloy AA5252. Additional microstructural information can be obtained from phase-contrast tomography (PCT) [29], which enables precise spatial identification of second-phase particles in this material. By correlating these two imaging techniques, the authors demonstrated that AGG cannot be attributed to inhomogeneity in the distribution of pinning particles. Instead, AGG appears to be correlated with the abnormal grain being bounded by GBs with above-average misorientation angles and neighbor grains of smaller-than-average size [26].

The primary objective of this study is to deepen the analysis of GB migration during AGG in the AA5252 specimen presented in [26] by systematically investigating the local influence of GB morphology on GB velocity. In particular, we extend the analysis of the relationship between mean curvature and GB velocity beyond the conventional curvature-driven migration picture. However, a major obstacle in the determination of GB morphology arises from the voxel-based nature of the microstructural maps generated by DCT and PCT, whose discrete structure complicates the accurate determination of GB mean curvatures and velocities. To mitigate these computational limitations, we implemented a continuous rather than discrete microstructural representation. Building on a modified version of the framework proposed in [30], in which each GB is represented as a continuous surface representation, we are able to compute the mean curvature and velocity at any given point on a GB. By additionally

investigating the dynamic interactions and constraints imposed by GBs connected via triple junctions, we aim to resolve (apparent) discrepancies between experimental observations and predictions of conventional GB migration models, in particular when considering AGG.

2. Materials and image acquisition

This section details the materials and experimental methodologies employed in the study.

2.1. Image acquisition and preprocessing of grain microstructures

The 3D microstructure mappings were carried out on a cylindrical aluminum alloy AA5252 specimen with a diameter of 0.8 mm, extracted from a plate-shaped specimen by spark erosion. Prior to extraction, the plate was cold-rolled to a thickness reduction of 80%, followed by recrystallization via two consecutive annealing steps of 30 min at 400 °C in a custom-built vertical furnace. Subsequently, the specimen was subjected to 15-minute annealing intervals at 500 °C, reaching a total annealing time of 90 min at this temperature. Additional details on specimen preparation and thermal treatment are provided in [26]. After each annealing interval, the 3D microstructure was characterized by DCT at beamline ID11 of the European Synchrotron Radiation Facility (ESRF). Subsequently, the grain maps were registered, and the tracking algorithm described in [31, 32] was applied to the grain maps to ensure that individual grains retain the same label across subsequent time steps. For a detailed description of the imaging and data processing procedures, see [26]. In total, six DCT grain maps with a resolution of 1.78 µm per voxel side length were reconstructed with sufficient completeness and quality for quantitative analysis. Figure 1 shows the reconstructed 3D microstructure at three different time steps, with the abnormally growing grain of particular interest in this paper labeled G^{a}.

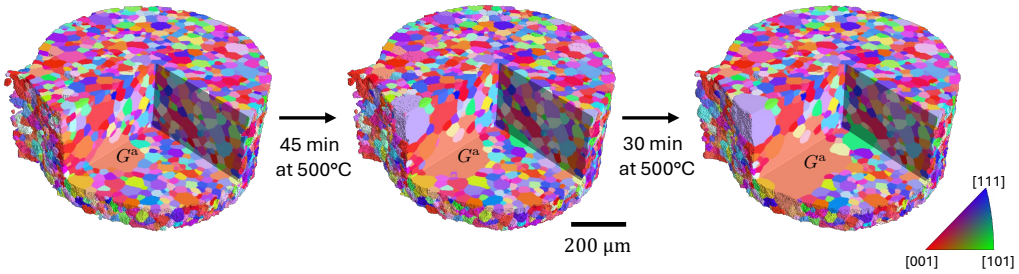


FIGURE 1. Microstructural evolution in the AA5252 alloy for three selected annealing intervals. The specimen was annealed at 500 °C for 90 min, with the first DCT measurement acquired after 15 min and subsequent measurements performed at 15-min intervals. A wedge-shaped portion of the cylindrical specimen has been cut out to expose internal GBs. The abnormally growing grain G^{a} is shown in orange. Grains are colored according to their crystallographic orientation using the inverse pole figure (IPF) color coding scheme (lower right inset).

2.1.1. *Description of 3D image data*

Formally, the image obtained from DCT after processing is defined for each annealing time step $t \in \{15, 30, 45, 60, 75, 90\,\mathrm{min}\}$ as a mapping $I_t \colon W \to \{0, 1, 2, \ldots, n_t\}$. Due to the registration process, all images have the same domain $W \subset \mathbb{Z}^3 = \{\ldots, -1, 0, 1, \ \ldots\}^3$, which is given by $W = W' \cap \mathbb{Z}^3$ for a bounded cubic sampling window $W' \subset \mathbb{R}^3$, and $n_t \in \mathbb{N}$ denotes the number of grains at time step t. In this framework, the image I_t assigns each voxel $x \in W$ to a specific

grain label or to the background; i.e., I_t is given by

$$I_t(x) = \begin{cases} i, & \text{if } x \text{ belongs to the } i\text{th grain for } i \in \{1, 2, \ldots, n_t\}, \\ 0, & \text{otherwise,} \end{cases} \tag{1}$$

for each $x \in W$. The ith grain at time t is given by the set of voxels $G_{i,t} = \{x \in W \colon I_t(x) = i\}$.

2.1.2. *Preprocessing of image data*

The images obtained from the DCT measurements exhibit various artifacts, including voxels incorrectly classified as background despite being located within the specimen, as well as isolated voxels erroneously assigned to grains to which they do not physically belong. Such artifacts can adversely affect the accuracy of GB surface representations. To mitigate these artifacts, each image I_t is preprocessed prior to further analysis.

In a first step, isolated voxels are identified that were erroneously assigned to grains to which they do not belong. This is accomplished by determining, for each grain, all connected components of voxels assigned to the corresponding grain label, employing an 18-neighborhood connectivity criterion. Two voxels x_1 and x_2 are considered neighbors if $\|x_1 - x_2\| \leq \sqrt{2}$, where $\|\cdot\|$ denotes the Euclidean norm in $\mathbb{R}^3$. In cases where multiple disconnected components are detected for a single grain, only the largest connected component is retained, while all smaller components are reclassified as isolated voxels. A similar procedure is applied to identify voxels that were assigned erroneously to the background, despite being located within the polycrystalline specimen. In particular, all connected components of the voxels labeled as background by I_t are detected, and only the largest connected component is preserved; all smaller disconnected components are reclassified as isolated voxels. This preprocessing step results in a corrected image $I_{c,t} \colon W \to \{-1, 0, 1, 2, \ldots, n_t\}$, where each voxel $x \in W$ is assigned to a specific grain, to the background label (0) or to the isolated voxel label (-1).

In a second step, isolated voxels are reassigned to surrounding grains. For this purpose, a marker-based watershed algorithm [33] is employed. This algorithm is a region-growing algorithm, meaning that the image to which the algorithm is applied is treated as a topographic map, with region growing starting from a predefined set of markers. The regions grow until they meet. In this context, these regions correspond to the grains, which enables us to assign isolated voxels to specific grains. As the marker for the watershed algorithm, the marker image $\widetilde{I}_{c,t} \colon W \to \{0, 1, 2, \ldots, n_t\}$ is utilized, which corresponds to the corrected image $I_{c,t}$ with isolated voxels excluded. Formally, the image $\widetilde{I}_{c,t}$ is given by $\widetilde{I}_{c,t}(x) = I_{c,t}(x)$ if $I_{c,t}(x) \geq 0$, otherwise $\widetilde{I}_{c,t}(x) = 0$ for each $x \in W$. The image used for the watershed algorithm is given by the negative Euclidean distance transform [34, 35] of the binary image $I_{b,t} \colon W \to \{0, 1\}$ that identifies isolated voxels and background, where $I_{b,t}(x) = 1$ if $I_{c,t}(x) \leq 0$, otherwise $I_{b,t}(x) = 0$, for each $x \in W$. The application of the marker-based watershed algorithm to the negative Euclidean distance transform of $I_{b,t}$ corresponds heuristically to a region-growing procedure in which the markers grow at a speed given by the negative Euclidean distance transform, progressively consuming the isolated voxels. From this algorithm, we obtain an image $I_{s,t} \colon W \to \{1, 2, \ldots, n_t\}$, which assigns each voxel $x \in W$ to a specific marker in the marker image $\widetilde{I}_{c,t}$. Each region consisting of connected voxels, assigned to a marker by $I_{s,t}$, then corresponds to a grain. To correctly represent the actual background of the specimen, the values of $I_{s,t}$ are reset to zero for all voxels $x \in W$ where $I_{c,t}(x) = 0$.

2.1.3. *Extraction of GBs from image data*

A GB in a polycrystalline material represents an interface between two adjacent grains in the underlying grain structure. By utilizing the image data $I_{s,t}$ at time step t, we extract the GB between two adjacent grains $G_{i,t}, G_{j,t} \subset W$ for any pair $i, j \in \{1, \dots, n_t\}$ with $i \neq j$ by identifying voxels in W in the neighborhood of both grains. More precisely, the GB can be described by the image $I_{B_{ij,t}} \colon W \to \{0, 1\}$, with

$$I_{B_{ij,t}}(x) = \begin{cases} 1, & \text{if } I_{s,t}(x) = i \text{ and } \#M_{j,t}(x) \geq 1 \text{ or } I_{s,t}(x) = j \text{ and } \#M_{i,t}(x) \geq 1, \\ 0, & \text{otherwise,} \end{cases} \tag{2}$$

for each $x \in W$, where $\#$ denotes cardinality and $M_{k,t}(x) = \{y \in W \colon \|x - y\| = 1 \text{ and } I_{s,t}(y) = k\}$ is the 6-neighborhood of the voxel $x \in W$ within the grain $G_{k,t}$ for $k \in \{1, \dots, n_t\}$. Then, the GB can be represented by the set of voxels $B_{ij,t} = \{x \in W \colon I_{B_{ij,t}}(x) = 1\}$, with $n_{B_{ij,t}} = \#B_{ij,t}$ selecting the number of voxels belonging to this GB. In the following, we refer to all voxels belonging to $B_{ij,t}$ as *GB points*.

Of particular interest in the analysis of GB migration are triple junctions (curves at which three GBs intersect). Therefore, we consider the set of voxels $J_{ij,t} \subset W$ belonging to the triple junctions associated with a GB $B_{ij,t}$, which is given by

$$J_{ij,t} = \bigcup_{k \in \{1,2,\dots,n_t\} \setminus \{i,j\}} B_{ij,t} \cap B_{ik,t}. \tag{3}$$

2.2. **Image acquisition and registration of second-phase particles**

To identify second-phase particles in the AA5252 specimen, time-resolved PCT measurements were conducted and afterwards temporally and spatially aligned with the DCT measurements in [26]. Subsequently, the second-phase particles were segmented from the PCT data as described in [26], enabling the detection of particle–GB interactions and their influence on GB migration.

To describe each particle, its center coordinates and corresponding volume-equivalent diameter were determined prior to spatially aligning the PCT and DCT measurements. Then, the coordinates of particle centers were transformed using the rigid transformations applied to align the PCT and DCT measurements as described in [26]. This results in a set $E_t = \{e_t^{(i)}\}_{i=1}^{n^{E_t}} \subset \mathbb{R}^3$ of second-phase particles detected for each time step t, where each $e_t^{(i)} \in \mathbb{R}^3$ denotes the coordinates of the ith particle center, and $n^{E_t} \geq 1$ is the overall number of particles identified at time t. It should be noted that, although potential segmentation artifacts in the processing of PCT data may result in variations in the spatial distribution of detected particles across the annealing intervals, the analysis of the spatial distribution of particles in [26] found second-phase particles to have remained stationary throughout the annealing process.

3. Representation and tracking of GBs

The image data of polycrystalline microstructures are usually specified in a discrete, voxel-based manner, which provides easy access to the volume of individual grains and the grain size distribution. However, voxelized representations of microstructures introduce problems in the analysis of GBs and their descriptors, like surface area or mean curvature. To address this challenge, we extracted each GB from the image data and represented it as a continuous surface.

In this study, we modify the methodology introduced in [30] to construct surface representations based on spherical harmonics [36] rather than smoothing thin-plate splines. This alternative approach enables the representation of GBs associated with "island" grains and grains having peninsula-shaped boundaries. Such GBs begin to curve back on themselves, a phenomenon that occurs in particular in the case of AGG, and for such GBs the method introduced in [30] remains applicable only locally. In addition, the spherical harmonics–based approach is conceptually simpler and provides improved accuracy in GB representation, particularly in regions near triple junctions. Additional details are provided in Appendix A on the limitations of thin-plate splines for representing the GBs of island grains, and a comparative evaluation of both approaches is given there, as well.

3.1. **Spherical harmonics representation**

Spherical harmonics have previously been used in applications comparable to the present study to model the outer shell of bounded 3D objects from volumetric image data, including particles in cathodes of lithium-ion batteries [37, 38], quartz and glass particles [39], as well as objects observed in biological image data [40]. In the following, we describe the use of spherical harmonics for modeling a GB as a subset of the outer shell of a grain.

The modeling procedure for the outer shape of a 3D object follows the approach developed in [36]. For this, we assume that the object is star-shaped, which means that the object has a so-called star point, from which the line segment to any other point of the object is fully contained within the object. Then, the outer shell of the object with star point $c = (c_\mathrm{x}, c_\mathrm{y}, c_\mathrm{z}) \in \mathbb{R}^3$ can be described by a radius function $r\colon [0, 2\pi) \times [0, \pi] \to [0, \infty)$, where a point $p = (p_\mathrm{x}, p_\mathrm{y}, p_\mathrm{z}) \in \mathbb{R}^3$ on the outer shell can be expressed in Cartesian coordinates by

$$p_\mathrm{x} = c_\mathrm{x} + r(\theta, \phi)\sin(\theta)\cos(\phi), \quad p_\mathrm{y} = c_\mathrm{y} + r(\theta, \phi)\sin(\theta)\sin(\phi), \quad p_\mathrm{z} = c_\mathrm{z} + r(\theta, \phi)\cos(\phi) \tag{4}$$

for some $\theta \in [0, 2\pi)$ and $\phi \in [0, \pi]$. The outer shell is given by the set

$$O = \{c + r(\theta, \phi)(\sin(\phi)\cos(\theta), \sin(\phi)\sin(\theta), \cos(\phi))\colon (\theta, \phi) \in [0, 2\pi) \times [0, \pi]\}. \tag{5}$$

In practice, the radius function r is generally unknown. For image data, observations of r are available only at discrete locations on the outer shell of a 3D object. Therefore, a continuous approximation of the radius function is obtained by introducing a parametric representation $r_w\colon [0, 2\pi) \times [0, \pi] \to \mathbb{R}$ given by

$$r_w(\theta, \phi) = \sum_{k=0}^{L} \sum_{m=-k}^{k} w_k^m Y_k^m(\theta, \phi), \tag{6}$$

where the entry w_k^m of the parameter vector w is called a spherical harmonics coefficient, and the function Y_k^m is called a spherical harmonics function for any pair of integers k, m with $-k \leq m \leq k$ and $k \geq 0$. For technical details on the construction and fitting of such a radius function, see [36]. For practical reasons, the spherical harmonics series expansion considered in Eq (6) is limited to a maximum degree of $L > 0$. If L increases unboundedly, it is possible to gain a better and better approximation r_w of the radius function r.

For notational simplicity, a GB $B_{ij,t}$ will be denoted by B_t, since an identical surface representation procedure is applied to all GBs. To represent a GB B_t using spherical harmonics, we first extract the GB from the image data as described in Section 2.1.3. Then, the GB B_t is represented by a discrete set $\Omega_{B_t} \subset [0, 2\pi) \times [0, \pi]$ before being modeled as a continuous surface representation $S_t \subset \mathbb{R}^3$. By expressing each point in B_t in Cartesian coordinates as given in

Eq. (4), we transform the set B_t into spherical coordinates. This results in the set Ω_{B_t} given by

$$\Omega_{B_t} = \{(\theta, \phi) \in [0, 2\pi) \times [0, \pi] \colon c_{B_t} + r(\theta, \phi)(\sin(\phi)\cos(\theta), \sin(\phi)\sin(\theta), \cos(\phi)) \in B_t\}. \quad (7)$$

with star point $c_{B_t} \in \mathbb{R}^3$. The star point c_{B_t} is determined by fitting an ellipsoid to the points in B_t, where the ellipsoid fitting procedure for voxelized image data closely follows the approach proposed in [41], adapted for GB-specific fitting as described in [30]. The center of the fitted ellipsoid is selected as the star point c_{B_t}. Then, by determining an appropriate estimate $\widehat{w}$ for the parameter vector w of the radius function given in Eq. (6), we obtain the continuous surface representation S_t,

$$S_t = \{c_{B_t} + r_{\widehat{w}}(\theta, \phi)(\sin(\phi)\cos(\theta), \sin(\phi)\sin(\theta), \cos(\phi)) \colon (\theta, \phi) \in \Omega_t\}, \quad (8)$$

for some continuous domain $\Omega_t \subset [0, 2\pi) \times [0, \pi]$. In order to obtain a suitable domain Ω_t, we construct an alpha shape of Ω_{B_t}, computed using the MATLAB function `alphaShape` (see [42, 43] for additional details). Empirically, choosing the parameter $L = 5$ yields sufficient smoothing to ensure a robust representation of GBs obtained from noisy image data. Recall that the complete outer shell of a grain can be represented using spherical harmonics. However, because each GB is modeled as a subset of the grain's outer shell, the grain itself does not need to be star-shaped. This is particularly important in the context of abnormally growing grains, where the star-shaped assumption is often violated.

The construction of a surface representation of a GB from image data enables the quantification of its local migration dynamics and morphological characteristics. For computational reasons, we discretize the (continuous) surface representation of a GB to determine a finite number of points at which the local migration dynamics and morphological characteristics are subsequently evaluated. Such a finite subset $S_{\mathrm{d},t}$ of the surface representation S_t of a GB is given by

$$S_{\mathrm{d},t} = \{c_{B_t} + r_{\widehat{w}}(\theta, \phi)(\sin(\phi)\cos(\theta), \sin(\phi)\sin(\theta), \cos(\phi)) \colon (\theta, \phi) \in \Omega_{B_t}\}. \quad (9)$$

It is important to note that, once the corresponding (continuous) surface representation of a GB has been discretized, the meaning of descriptors like the local mean curvature or the normal vector (see Section 4) to points on the surface becomes unclear. To address this issue, we instead associate the descriptors of points on the discretized surface representation $S_{\mathrm{d},t}$ with the descriptor values of these points obtained from the corresponding continuous surface representation S_t.

3.2. **Tracking of GBs**

By constructing surface representations of a GB from image data over two consecutive time steps, we are able to perform a pointwise tracking of the time-resolved representations and thereby quantify local migration dynamics. The pointwise tracking procedure follows the methodology proposed in [30]. More precisely, each GB is observed over two successive time steps, t and $t + \Delta t$, with $t \geq 0$, $\Delta t > 0$, then extracted from the corresponding image data, and finally represented by the surfaces S_t and $S_{t+\Delta t}$ given by Eq. (8). A pointwise correspondence is then established between the discrete point sets $S_{\mathrm{d},t}$ and $S_{\mathrm{d},t+\Delta t}$ associated with S_t and $S_{t+\Delta t}$—see Eq. (9)—where each $p_t \in S_{\mathrm{d},t}$ is uniquely associated with a corresponding point $p_{t+\Delta t} \in S_{\mathrm{d},t+\Delta t}$.

4. Descriptors of GBs

The surface representation of GBs introduced in Section 3 provides a framework for describing each GB with respect to its morphology and migration behavior, including the influence of second-phase particles on GB migration as well as the crystallographic texture derived from image data. In the present section, we introduce various descriptors of GBs, where for notational simplicity, the GB between two adjacent grains $G_{i,t}$ and $G_{j,t}$ is denoted by B_t instead of $B_{ij,t}$.

Recall that GBs are extracted from image data as stated in Section 2.1.3 and subsequently represented by surfaces as described in Section 3. The latter procedure yields the surface representation S_t for B_t by means of Eq. (8), with the discretized version $S_{\mathrm{d},t}$ given by Eq. (9). Note that the precision of GB surface representations is reduced near triple junctions due to the smaller number of points available for surface fitting. Consequently, local descriptors are evaluated exclusively for GB points located a sufficient distance from these junctions: following the approach of [30], local descriptors are computed only for points p_t within the discrete subset $S_{\mathrm{d},d_{\min},t} \subset S_{\mathrm{d},t}$ given by

$$S_{\mathrm{d},d_{\min},t} = \{p \in S_{\mathrm{d},t} \colon \min_{x \in J_t} \|p_t - x\| \geq d_{\min}\} \tag{10}$$

for some adjustable minimum distance $d_{\min} \geq 0$, where J_t denotes the set of voxels corresponding to the triple junctions associated with the GB, as defined in Eq. (3). Thus, GB characterization is restricted to points that are located at least a distance $d_{\min}$ from the triple junctions.

4.1. Morphological descriptors

GB size. The size of a GB is described by its surface area, where the area is approximated by the surface area $A_t \in [0, \infty)$ of its surface representation S_t. Using the spherical harmonics representation considered in Section 3.1, the surface area A_t is computed as stated in [36] by

$$A_t = \int_{\Omega_t} r_{\widehat{w}}(\theta,\phi) \left(\left(\frac{\partial}{\partial \phi} r_{\widehat{w}}(\theta,\phi) \right)^2 + \left(\frac{\partial}{\partial \theta} r_{\widehat{w}}(\theta,\phi) \right)^2 \sin^2(\theta) + r_{\widehat{w}}^2(\theta,\phi) \sin^2(\theta) \right)^{1/2} \mathrm{d}\phi \, \mathrm{d}\theta, \tag{11}$$

where Ω_t denotes the set of angles of the surface representation S_t (Eq. (8)). The integral in Eq. (11) is approximated by Monte Carlo integration [44] over the set O_{B_t} given by Eq. (7).

GB shape. The shape of the GB is described by its mean curvature. Note that the spherical harmonics representation enables the computation of the local mean curvature $H_t(p_t) \in \mathbb{R}$ for each point $p_t \in S_{\mathrm{d},d_{\min},t}$. For details on computing local mean curvature values, the reader is referred to [36]. The mean curvature $\overline{H}_t \in [0, \infty)$ of the GB B_t is then computed by

$$\overline{H}_t = \left| \frac{1}{\# S_{\mathrm{d},d_{\min},t}} \sum_{p_t \in S_{\mathrm{d},d_{\min},t}} H_t(p_t) \right|, \tag{12}$$

where $|\cdot|$ denotes the absolute value.

4.2. Misorientation angle – a crystallographic descriptor of GBs

Note that the crystallographic texture of each grain is given by a rotation matrix relative to a reference coordinate system [45]. More precisely, from the DCT image data stated in Section 2.1.1, voxel-wise information on the local crystallographic orientations of the specimen is obtained, which is used to determine the crystallographic orientation of each grain. For a GB between two grains, the difference in the orientation of the grains is quantified by the

misorientation angle $\overline{\varphi}_t \in [0, 62.8°)$. Details of the procedure by which misorientation angles are computed can be found in [45].

4.3. **Descriptor of GB migration**

In the analysis of GB migration, we distinguish between two classes of GBs: *nonvanishing* and *vanishing* GBs. This distinction is based on whether a given GB is present in the image data over two consecutive time steps. For both classes, the GB can be represented at the initial time step using the surface representation framework described above, enabling the description of its morphology and crystallography. However, only nonvanishing GBs enable a direct examination of local migration behavior, since tracking the migration of GB points requires surface representations at two successive time steps. In the following, we detail the different procedures used to analyze the migration behavior of these two GB classes by determining the velocity $v_t \in [0, \infty)$ of each GB over the interval from time step t to $t + \Delta t$.

4.3.1. *Migration of nonvanishing GBs*

Local GB velocity. The local migration of a GB is described by the displacement of points on its discretized surface representations $S_{\mathrm{d},t}$ and $S_{\mathrm{d},t+\Delta t}$. By pointwise assignments as described in Section 3, the displacement vector $D(p_t) \in \mathbb{R}^3$ of each point $p_t \in S_{\mathrm{d},t}$ to the assigned point $p_{t+\Delta t} \in S_{\mathrm{d},t+\Delta t}$ is given by $D(p_t) = p_{t+\Delta t} - p_t$. Consequently, the local velocity $v_{\mathrm{loc},t}(p_t)$ at $p_t \in S_{\mathrm{d},t}$ is given by $v_{\mathrm{loc},t}(p_t) = \|D(p_t)\|/\Delta t$.

Local GB migration direction. Furthermore, we analyze how much the migration direction of a GB point deviates from its normal direction. This enables assessing whether a GB point migrates toward its center of curvature. The discrepancy between migration direction and normal direction of a GB point p_t is described by the displacement angle $\alpha_{\mathrm{nv},t}(p_t) \in [0°, 180°]$ between the displacement vector $D(p_t)$ and the displacement vector $N(p_t) \in \mathbb{R}^3$ in normal direction. For more details, we refer to [30]. A visualization of the determination of the local migration direction of a nonvanishing GB is provided in Figure 2(a).

4.3.2. *Migration of vanishing GBs*

Certain GBs disappear over time because the associated grains are not adjacent anymore or because one of the grains is no longer observable in the image data at later time steps. However, these boundaries are still of interest, as they potentially exhibit migration characteristics that differ from those of GBs that persist throughout the observation period.

GB velocity. The migration behavior of vanishing GBs is quantified using the volume exchanged between pairs of neighboring grains, where the exchanged volume $V_{\mathrm{ex},t} \in [0, \infty)$ during a time step Δt is determined from the image data by counting the voxels transferred between the two grains considered. Using the exchanged volume to describe the migration of a GB is similar to the approach published in the literature of computing the GB velocity from the ratio of the exchanged volume to the average interfacial area between the same grain pair at the two time steps, normalized by Δt [46, 47]. However, for vanishing GBs, the average interfacial area cannot be determined. Thus, for a vanishing GB we estimate the boundary velocity $v_{\mathrm{ex},t} \in [0, \infty)$ from

$$v_{\mathrm{ex},t} = \frac{V_{\mathrm{ex},t}}{\frac{1}{2} A_t \Delta t}, \tag{13}$$

where the GB surface area A_t is given by means of Eq. (11). Additional details concerning Eq. (13), particularly regarding the constant 1/2 in Eq. (13), are provided in Appendix B.

Local GB migration direction. A vanishing GB can still be represented by a surface as described in Section 3; however, such a GB is observable at only a single time step, preventing a pointwise correspondence of GB points between consecutive time steps. Consequently, the local GB migration direction cannot be determined using the approach applied to nonvanishing GBs. Instead, the migration direction of a GB point p_t on a vanishing GB with surface representation S_t is described by the displacement angle $\alpha_{\mathrm{v},t} \in [0°, 180°]$, which we define as the angle between the normal vector $N(p_t)$ and the vector pointing from p_t to the center of mass of the grain being consumed. The direction of $N(p_t)$ is chosen such that the angle between $N(p_t)$ and the vector pointing from p_t to the center of mass of the grain being consumed is minimized. A visualization of the determination of the local migration direction of a vanishing GB is provided in Figure 2(b).

4.3.3. *Velocity and migration direction of GBs*

The velocity of a GB $v_t \in [0, \infty)$ is approximated in the case of a nonvanishing GB by the mean value of local velocity values $\overline{v}_{\mathrm{loc},t} \in [0, \infty)$ at each GB point $p_t \in S_{\mathrm{d},d_{\min},t}$; i.e., the value of $\overline{v}_{\mathrm{loc},t}$ is computed from

$$\overline{v}_{\mathrm{loc},t} = \frac{1}{\#S_{\mathrm{d},d_{\min},t}} \sum_{p_t \in S_{\mathrm{d},d_{\min},t}} v_{\mathrm{loc},t}(p_t). \tag{14}$$

In case of a vanishing GB, the velocity v_t is approximated by the velocity given in Eq. (13). To quantify the migration direction of a GB represented by the surface $S_{\mathrm{d},d_{\min},t}$, we consider the mean displacement angle $\overline{\alpha}_t \in [0°, 180°]$, which is approximated in the case of a nonvanishing GB by the angle

$$\overline{\alpha}_{\mathrm{nv},t} = \frac{1}{\#S_{\mathrm{d},d_{\min},t}} \sum_{p_t \in S_{\mathrm{d},d_{\min},t}} \alpha_{\mathrm{nv},t}(p_t) \tag{15}$$

and in the case of a vanishing GB by the angle

$$\overline{\alpha}_{\mathrm{v},t} = \frac{1}{\#S_{\mathrm{d},d_{\min},t}} \sum_{p_t \in S_{\mathrm{d},d_{\min},t}} \alpha_{\mathrm{v},t}(p_t). \tag{16}$$

4.3.4. *Migration of connected GBs*

In addition, this study investigates the influence of GB network effects on the migration of individual GBs. In a polycrystalline material, GBs constitute an interconnected topological network in which individual boundaries are connected through triple junctions. Consequently, the migration of a specific GB is kinematically constrained by the mobility of its adjacent GBs, which we will be referred to as *connected GBs*. To quantify this collective behavior, we define the mean velocity $\overline{v}_{\mathrm{con},t} \in [0, \infty)$ of connected GBs. This value is derived by computing the mean value of the individual velocities of all adjacent GBs, accounting for their classification as either nonvanishing or vanishing GB (see Sections 4.3.1 and 4.3.2, respectively). The value of $\overline{v}_{\mathrm{con},t}$ is then used to describe the influence of the GB network on the migration behavior of a specific GB—that is, the influence of the migration behavior of GBs connected to that GB via triple junctions—and is referred to as *connected GB velocity*.

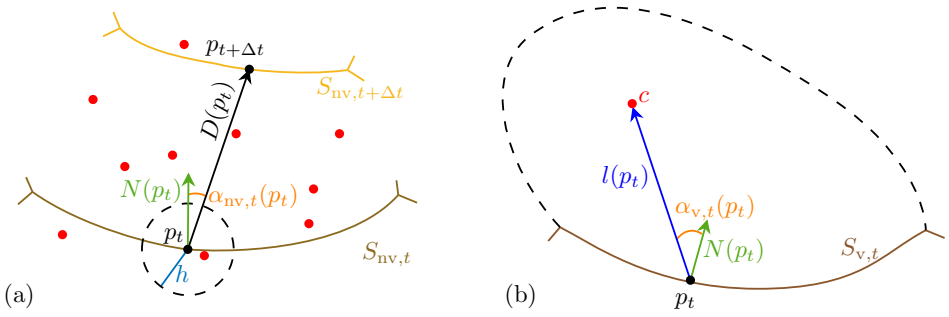


FIGURE 2. 2D illustration of the determination of the local migration direction of a GB point p_t (black dot) for (a) a nonvanishing GB and for (b) a vanishing GB. In case of a nonvanishing GB, a GB point p_t (black dot) located on the surface representation S_t^{nv} (brown lines) migrates with displacement vector $D(p_t)$ to the point $p_{t+\Delta t}$ located on the surface representation $S_{t+\Delta t}^{\mathrm{nv}}$ (yellow lines). The migration angle $\alpha_{\mathrm{nv},t}(p_t)$ corresponds to the angle between the normal vector $N(p_t)$ (green arrow) and $D(p_t)$. In case of a vanishing GB, the migration angle $\alpha_{\mathrm{v},t}(p_t)$ of a GB point p_t (black dot) on the surface representation S_t^{v} (brown curve) corresponds to the angle between the normal vector $N(p_t)$ (green arrow) and vector $l(p_t)$ (blue arrow) from p_t to the center of mass c (red dot) of the consumed grain (region enclosed by the black dashed line and S_t^{v}). In addition, in (a), the influence of second-phase particles (red dots) on the local migration behavior of p_t is visualized.

4.4. **Descriptors for the influence of second-phase particles on GB migration**

Second-phase particles are typically much smaller than the average grain size, yet they are capable of interacting with migrating GBs. During such interactions, particles can exert drag forces that decelerate or even immobilize the GB. In [26] the pinning effect of such particles on boundary migration in AA5252 was examined at the GB level. To additionally investigate the local pinning effect at the level of individual GB points, we introduce two descriptors that enable a quantitative characterization of the influence of second-phase particles on local GB migration behavior.

4.4.1. *Spatial influence factor*

We consider the pinning effect of particles on a GB point p_t by quantifying the number of particles within a ball $B(p_t, h) = \{y \in \mathbb{R}^3 \colon \|y - p_t\| \leq h\}$ with radius $h > 0$ centered at p_t. Each particle contributes according to its Euclidean distance from p_t. More precisely, for p_t we consider the so-called *spatial influence factor* $\lambda_{h,t} \colon \mathbb{R}^3 \to [0, \infty)$, which is given by

$$\lambda_{h,t}(p_t) = \frac{1}{\#\{e \in E_t \cap B(p_t, h)\}} \sum_{e \in E_t} k\left(\frac{\|p_t - e\|}{h}\right), \tag{17}$$

where E_t is the set of particle centers at time t, and $k \colon \mathbb{R} \to [0, \infty)$ denotes the Epanechnikov kernel [48] given by $k(x) = \frac{3}{4}(1 - x^2)\mathbb{1}_{[0,1]}(x)$ for each $x \in \mathbb{R}$, where $\mathbb{1}_A : \mathbb{R} \to \{0, 1\}$ denotes the indicator of a set $A \subset \mathbb{R}$, i.e., $\mathbb{1}_A(x) = 1$ if $x \in A$, otherwise $\mathbb{1}_A(x) = 0$. The choice of this kernel is motivated by its compact support, which limits the influence of particles on a GB point to those whose centers are located within a distance of at most h. In particular, for a GB point p_t and a particle with center e satisfying $0 < \|p_t - e\| < h$, the kernel function evaluates to a positive value, i.e., $k(\|p_t - e\|/h) > 0$. Consequently, the particle with center e exerts a

positive influence on p_t by contributing positively to the sum in Eq. (17). A visualization of the computation of the spatial influencing factor for a GB point is provided in Figure 2(a). For a given value of $h > 0$, the descriptor $\lambda_{h,t}$ considers the number of particles located within a ball with radius h and center p_t to influence the migration behavior of p_t.

4.4.2. *Mean spatial influence factor*

In addition, we consider an aggregated effect of particles on a GB. For a GB with restricted surface representation $S_{\mathrm{d},d_{\min},t}$ we compute the *mean spatial influence factor* $\overline{\lambda}_{h,t} \in [0,\infty)$ given by

$$\overline{\lambda}_{h,t} = \frac{1}{\#S_{\mathrm{d},d_{\min},t}} \sum_{p_t \in S_{\mathrm{d},d_{\min},t}} \lambda_{h,t}(p_t). \tag{18}$$

5. Results

Recall that in this study, GB migration in the AA5252 specimen is quantified using 3D image data acquired at consecutive 15-minute annealing intervals from annealing times of 15 to 90 min. To investigate the temporal evolution of the microstructure during annealing, GBs are extracted from the time-resolved image data (Section 2), represented as continuous surfaces (Section 3), and subsequently characterized by various descriptors for migrating GBs (Section 4). In particular, for each GB, we utilize the GB velocity v_t, mean displacement angle $\overline{\alpha}_t$, mean curvature $\overline{H}_t$ and misorientation angle $\overline{\varphi}_t$ to describe its migration behavior, migration direction, morphology and crystallographic texture, respectively. For investigating an effect of second-phase particles on GB migration behavior, we examine the mean spatial influence factor $\overline{\lambda}_{h,t}$. We distinguish GBs exhibiting a positive influence factor ($\overline{\lambda}_{h,t} > 0$)—that is, only GBs with at least one second-phase particle in their vicinity—from GBs exhibiting an influence factor $\overline{\lambda}_{h,t} = 0$ to focus on regions actively subjected to particle interactions. The parameter h used for the influence factors is chosen to be the mean volume-equivalent particle radius, resulting in $h = 1.88\,\mu\mathrm{m}$, as determined in [26]. This value is motivated by the model of the Zener pinning pressure [22], where particles of equal size with diameter $2r$ exert a pinning pressure on the GB if their centers of mass lie within a distance r from the corresponding GB.

In the following analysis, only GB points located at a minimum distance of 2 voxels from triple junctions are considered, i.e., $d_{\min} = 2$. Additional details concerning this minimal distance to triple junctions can be found in Section 4. For GBs to still manifest sufficient surface area to ensure statistical reliability, only GBs with a minimum number of 200 GB points are considered. This threshold is motivated by the rule of thumb proposed in [30] and adapted in Appendix A for the surface representation of GBs based on spherical harmonics. Furthermore, to assess a potential monotonic relationship between two descriptors of GBs, we utilize the Spearman correlation coefficient (SCC) [49] in the present paper. The SCC, which ranges from -1 to 1, quantifies the extent to which the relationship between two descriptors can be described by a monotonic function, where a value of 1 (or -1) indicates a perfectly monotonically increasing (or decreasing) relationship. Note that, when we refer to average values for a descriptor, the values in square brackets correspond to the 25th and 75th percentiles, respectively.

The microstructure of the AA5252 specimen is comprised of different GB types (see [26]). Slower-growing grains or grains that remain completely stagnant during annealing form boundaries referred to as matrix–matrix GBs. In contrast, there is an abnormally growing grain

$G^{\mathrm{a}} \subset W$ that already exhibits abnormal characteristics from the initial measurement, visualized in Figure 1. The boundaries associated with this grain are called abnormal GBs.

5.1. **Matrix-matrix GBs**

To illustrate the influence of crystallographic texture and second-phase particles on the migration of matrix–matrix GBs, Figure 3 presents box plots of GB velocity values v_t, grouped by values of (a) the misorientation angle $\overline{\varphi}_t$ and (b) the mean spatial influencing factor $\overline{\lambda}_{h,t}$. In the present paper, for all box plots, the boxes are bounded by the 25th and 75th percentiles, and the whiskers extend from the 10th to the 90th percentile. The mean and median values in each bin are marked by orange and brown lines, respectively. Figure 3(a) indicates that the distribution of $\overline{\varphi}_t$ values closely resemble the Mackenzie distribution [50] for randomly oriented cubic crystals, despite a weak peak around 10°. Thus, matrix-matrix GBs are more-or-less randomly distributed in misorientation space. Furthermore, these GBs consistently exhibit low v_t values with an average value of 0.090 µm min^{-1} [0.053 µm min^{-1}, 0.108 µm min^{-1}]. No significant migration is observed for this GB type, as the average velocity is below 0.356 µm min^{-1}, which corresponds to an average GB displacement of at least three voxels (each voxel has a side length of 1.78 µm) during a time interval of 15 min between successive grain mappings. Consequently, the migration of matrix–matrix GBs is negligible within the spatial and temporal resolution of the present analysis.

When considering the influence of particles, matrix-matrix GBs exhibit no visible differences in the distribution of v_t values when grouped by $\overline{\lambda}_{h,t}$ values (Figure 3(b)). Although each box plot contains roughly the same number of GBs, there is no difference between the mean and median values of the two groups. Furthermore, the SCC value of −0.023 between v_t and $\overline{\lambda}_{h,t}$ values indicates no significant monotonic relationship between GB velocity and second-phase particle influence.

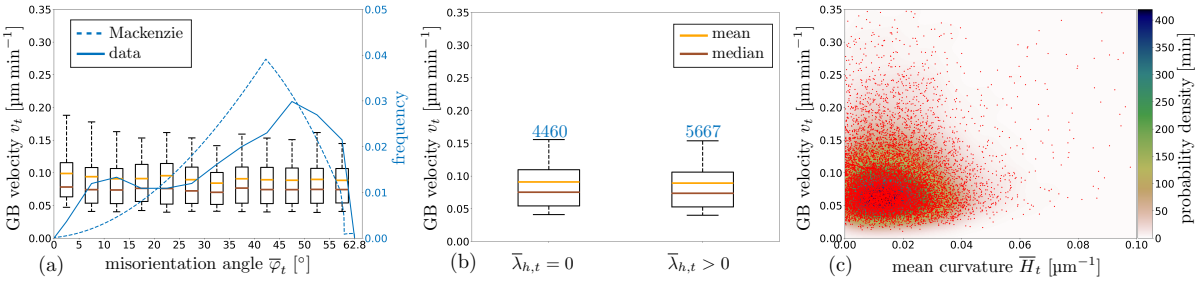


FIGURE 3. Results for matrix-matrix GBs. Box plots of GB velocity values v_t, grouped by values of (a) the misorientation angle $\overline{\varphi}_t$ and (b) the mean spatial influence factor $\overline{\lambda}_{h,t}$, with the frequency and number of GBs in each box plot indicated by the blue curve and blue number, respectively. The distribution of $\overline{\varphi}_t$ values is compared to the Mackenzie distribution (dashed blue line). Bivariate kernel density plots (c) of v_t and mean curvature $\overline{H}_t$ values. The measured values of $(v_t, \overline{H}_t)$ are plotted as red dots.

To analyze the GB morphology, in Figure 3(c) bivariate kernel density plots [51] of v_t and mean curvature $\overline{H}_t$ values are shown. Notably, matrix-matrix GBs exhibit an average mean curvature of approximately 0.018 µm^{-1} [0.008 µm^{-1}, 0.024 µm^{-1}]. In comparison, matrix grains exhibit an average mean diameter of approximately 30 µm across all annealing intervals, see [26], corresponding to an inverse mean grain radius of approximately 0.067 µm^{-1}. Thus, the average

mean curvature of matrix–matrix GBs is approximately 3.68 times smaller than the inverse mean grain radius, indicating that these GBs are predominantly flat. Furthermore, the SCC value of 0.025 between v_t and $\overline{H}_t$ indicates only a weak monotonic relationship between GB velocity and mean curvature for matrix-matrix boundaries.

5.2. **Abnormal GBs**

Compared to matrix–matrix GBs, abnormal GBs exhibit substantially faster migration, moving on average with a velocity of $0.781\,\mu m\,min^{-1}$ [$0.067\,\mu m\,min^{-1}$, $0.902\,\mu m\,min^{-1}$]. To illustrate the influence of crystallographic texture and second-phase particles on the migration behavior of abnormal GBs, Figure 4 presents box plots of GB velocity values v_t, grouped by values of (a) the misorientation angle $\overline{\varphi}_t$ and (b) the mean spatial influencing factor $\overline{\lambda}_{h,t}$. It can be observed that the distribution of $\overline{\varphi}_t$ values is similar to that of matrix-matrix GBs indicating no significant difference in crystallographic texture of these two GB types. However, in contrast to matrix-matrix GBs, abnormal GBs exhibit a larger difference in v_t values when grouped by $\overline{\lambda}_{h,t}$ values. In the absence of second-phase particles ($\overline{\lambda}_{h,t} = 0$), abnormal GBs take on an average velocity of $0.883\,\mu m\,min^{-1}$ [$0.065\,\mu m\,min^{-1}$, $1.113\,\mu m\,min^{-1}$] and a median velocity of $0.149\,\mu m\,min^{-1}$. On the other hand, GBs with $\overline{\lambda}_{h,t} > 0$ manifest an average velocity of $0.727\,\mu m\,min^{-1}$ [$0.068\,\mu m\,min^{-1}$, $0.805\,\mu m\,min^{-1}$] and a median velocity of $0.129\,\mu m\,min^{-1}$. However, the large standard deviation of v_t values compared to the average values within each group indicates the presence of outliers. Thus, the difference in the distribution of v_t values in the absence and presence of second-phase particles is mainly due to the presence of outliers in both groups, and the small discrepancy of median velocity values between both groups suggests that there is no measurable influence of second-phase particles on the migration behavior of abnormal GBs. This is further emphasized by an SCC of 0.011 between the values of v_t and $\overline{\lambda}_{h,t}$.

When analyzing the morphology of abnormal GBs, see Figure 4(c), where bivariate kernel density plots of v_t and $\overline{H}_t$ values are shown, we find these GBs to exhibit an average mean curvature of $0.027\,\mu m^{-1}$ [$0.017\,\mu m^{-1}$, $0.034\,\mu m^{-1}$], which is 1.44 times larger than the average mean curvature of matrix-matrix GBs. Thus, abnormal GBs are significantly more curved than matrix-matrix GBs. However, an SCC value of 0.013 between v_t and $\overline{H}_t$ values for abnormal GBs, compared to the SCC value of 0.025 for matrix-matrix GBs, does not indicate a stronger monotonic relationship between GB velocity and mean curvature for these GBs.

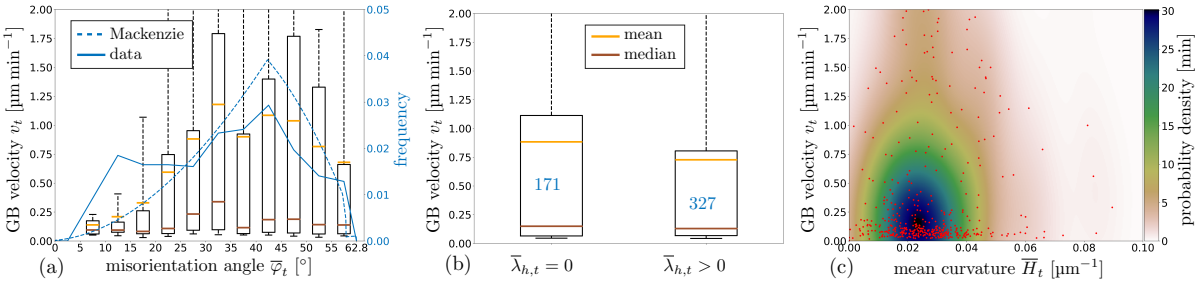


FIGURE 4. Results for abnormal GBs. Box plots of GB velocity values v_t, grouped by values of (a) misorientation angle $\overline{\varphi}_t$ and (b) the mean spatial influencing factor $\overline{\lambda}_{h,t}$, with the frequency and number of GBs in each box plot indicated by the blue curve and blue number, respectively. The distribution of $\overline{\varphi}_t$ values is compared to the Mackenzie distribution (dashed blue line). Bivariate kernel density plots (c) of v_t and mean curvature $\overline{H}_t$ values. The measured values of $(v_t, \overline{H}_t)$ are plotted as red dots.

5.2.1. *GB migration direction*

The migration direction of GBs is described by the value of the mean displacement angle $\overline{\alpha}_t$ (see Section 4.3.1). Small values of $\overline{\alpha}_t$ indicate migration in the direction of the mean normal vector, corresponding to migration toward the center of curvature, while values larger than 90° indicate displacement away from the center of curvature, i.e., such GBs exhibit anticurvature migration. A reliable determination of migration behavior—particularly the direction of migration—is possible only after the GB has undergone a measurable minimum displacement. To account for this, GBs are classified into *slow* and *fast* GBs based on a velocity threshold of $0.356\,\mu m\,min^{-1}$, which corresponds to an average GB displacement of at least three voxels (1.78 µm voxel side length) during a time interval of 15 min between successive grain mappings.

Figure 5 presents bivariate kernel density estimates of $\overline{\alpha}_t$ and v_t values for (a) slow and (b) fast abnormal GBs, where the dashed blue line at $\overline{\alpha}_t = 90°$ indicates the threshold for anticurvature GB migration. It can be observed that fast GBs consistently exhibit $\overline{\alpha}_t$ values below 90°, whereas slow GBs display a broader distribution of displacement angles. Approximately 67.8 % of the slow GBs have $\overline{\alpha}_t$ values below 90°, although the migration of these GBs is considered uncertain, since they move by an average of no more than three voxels. Furthermore, only two fast abnormal GBs exhibit $\overline{\alpha}_t$ values above 90°, and for approximately 40 % of the fast GBs $\overline{\alpha}_t$ lies below 30°.

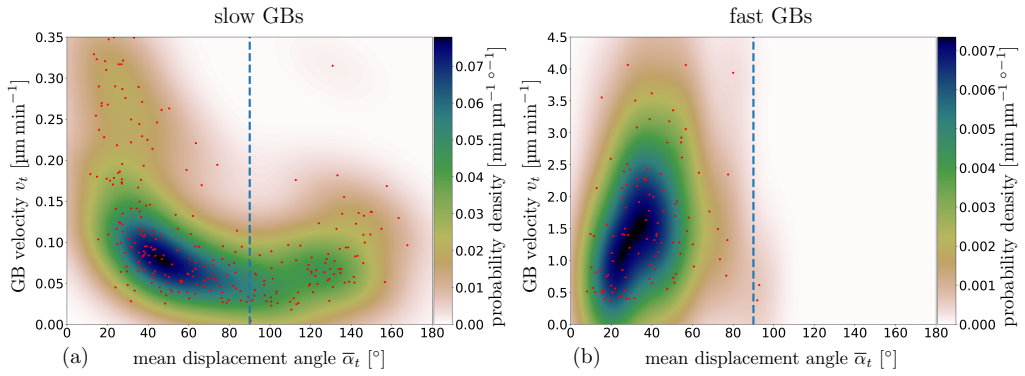


FIGURE 5. Bivariate kernel density estimates of GB velocity v_t and mean displacement angle $\overline{\alpha}_t$ values for (a) slow ($v_t < 0.356\,\mu m\,min^{-1}$) and (b) fast ($v_t \geq 0.356\,\mu m\,min^{-1}$) abnormal GBs. The measured values of $(\overline{\alpha}_t, v_t)$ are plotted as red dots, and values of $\overline{\alpha}_t > 90°$ (dashed blue line) correspond to anticurvature GB migration.

To further investigate the migration direction of abnormal GBs, in Figure 6 bivariate kernel density estimates of $\overline{\alpha}_t$ values and local mean curvature $\overline{H}_t$ are shown for (a) slow and (b) fast GBs. The dashed blue line at $\overline{\alpha}_t = 90°$ denotes the threshold for anticurvature GB migration. It can be observed that slow abnormal GBs, with an average mean curvature of $0.026\,\mu m^{-1}$ [$0.016\,\mu m^{-1}$, $0.032\,\mu m^{-1}$], are only slightly less curved than the fast abnormal GBs, which have an average mean curvature of $0.030\,\mu m^{-1}$ [$0.019\,\mu m^{-1}$, $0.038\,\mu m^{-1}$]. Furthermore, for the slow GBs there is no clearly visible relationship between the values of $\overline{H}_t$ and $\overline{\alpha}_t$. In contrast, Figure 6(b) suggests that fast GBs with larger $\overline{H}_t$ values tend to exhibit smaller $\overline{\alpha}_t$ values. Furthermore, the two fast abnormal GBs that show values of $\overline{\alpha}_t$ greater than 90° in Figure 6(a) have significantly lower $\overline{H}_t$ values than other fast abnormal GBs.

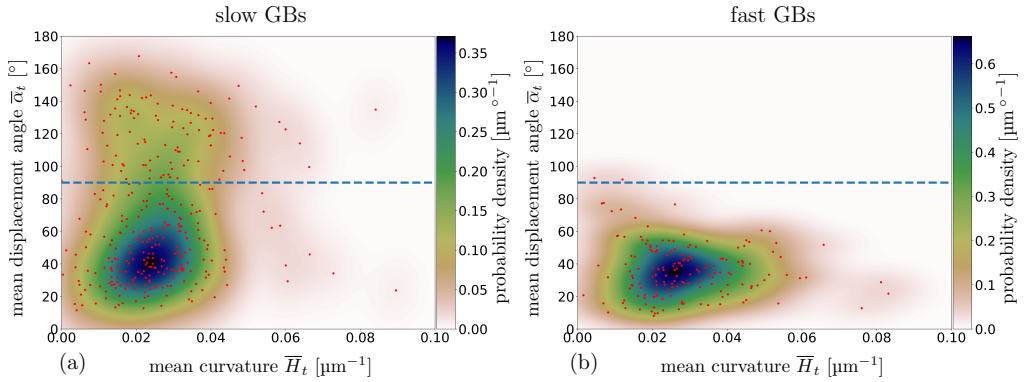


FIGURE 6. Bivariate kernel density estimates of mean displacement angle $\overline{\alpha}_t$ and local mean curvature $\overline{H}_t$ values for (a) slow ($v_t < 0.356\,\mu\text{m}\,\text{min}^{-1}$) and (b) fast ($v_t \geq 0.356\,\mu\text{m}\,\text{min}^{-1}$) abnormal GBs. The measured values of $(\overline{H}_t, \overline{\alpha}_t)$ are plotted as red dots, and values of $\overline{\alpha}_t > 90°$ (dashed blue line) correspond to anticurvature GB migration.

5.2.2. *Influence of GB connectivity on migration*

To quantify the influence of GB connectivity on the migration of abnormal GBs, we investigate the migration behavior of GBs connected to abnormal GBs via triple junctions. For this purpose, for each abnormal GB, we consider the connected GB velocity $\overline{v}_{\text{con},t}$ of the GBs connected via triple junctions to that GB (Section 4.3.4) and the number of connected GBs.

In Figure 7(a) the values of $\overline{v}_{\text{con},t}$ are plotted against the GB velocity values v_t, where the dashed blue line denotes equality of the two velocities. It can be observed that the GB velocity is highly correlated with the velocity of connected GBs, with SCC taking on a value of 0.78. Furthermore, in Figure 7(b), box plots of v_t values grouped by the number of connected GBs are shown. On average, each abnormal GB is connected to 6.9 ± 1.95 GBs. The leftmost box contains the fewest v_t values; however, it has the largest median value, indicating that GBs with a small number of connected GBs are more likely to migrate faster. In the other boxes, the value of v_t decreases as the number of connected neighbors increases, reflected by the decrease in mean and median values. The large difference between the mean and median values in the box plots is the result of outliers in the v_t values. We interpret these findings to imply that the likelihood of a given abnormal GB being connected to a slow GB increases somewhat with the number of such connections.

It is generally assumed that the inherent crystallographic texture of a polycrystal can initiate AGG [17–19], as high-angle GBs typically migrate faster than their low-angle counterparts. To quantify this effect, Figure 8(a) shows box plots of v_t values for abnormal GBs grouped by $\overline{\varphi}_t$ values. We distinguish between low-angle GBs with values $\overline{\varphi}_t \leq 15°$ and high-angle GBs with values $\overline{\varphi}_t > 15°$. It can be observed that low-angle GBs exhibit significantly lower v_t values than high-angle GBs, with an average velocity of $0.186\,\mu\text{m}\,\text{min}^{-1}$ [$0.062\,\mu\text{m}\,\text{min}^{-1}$, $0.173\,\mu\text{m}\,\text{min}^{-1}$] and a median value of $0.095\,\mu\text{m}\,\text{min}^{-1}$ for low-angle GBs, compared to an average velocity of $0.877\,\mu\text{m}\,\text{min}^{-1}$ [$0.067\,\mu\text{m}\,\text{min}^{-1}$, $1.253\,\mu\text{m}\,\text{min}^{-1}$] and a median value of $0.155\,\mu\text{m}\,\text{min}^{-1}$ for high-angle GBs. Additionally, bivariate kernel density estimates of $\overline{v}_{\text{con},t}$ and v_t values for low-angle and high-angle GBs in Figure 8(b) and (c) further reveal spatial velocity coupling across the GB network: on average, GBs connected to low-angle GBs migrate with a velocity similar to the GBs to which they are connected, while those connected to high-angle GBs exhibit elevated velocities.

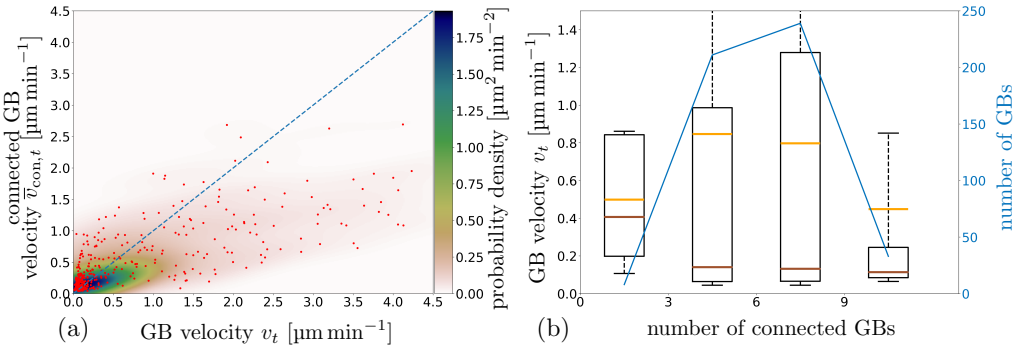


FIGURE 7. GB network effects on GB migration behavior of abnormal GBs. (a) Bivariate kernel density estimate of mean velocity values $\overline{v}_{\mathrm{con},t}$ of GBs connected to GBs with velocity v_t. The bisector line (dashed blue line) denotes equality of the values of $\overline{v}_{\mathrm{con},t}$ and v_t. The measured values of $(v_t, \overline{v}_{\mathrm{con},t})$ are plotted as red dots. (b) Box plots of v_t values and the number of connected GBs, with the number of GBs in each bin indicated by the blue curve. The rightmost box contains all v_t values of GBs with more than 9 connected GBs.

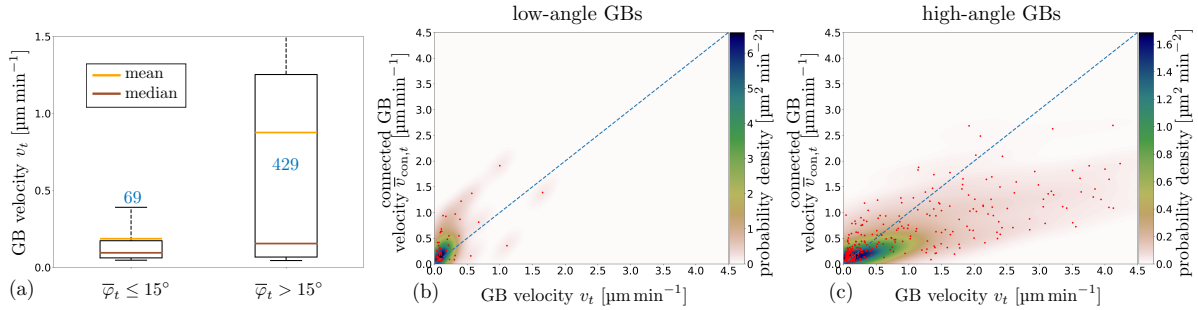


FIGURE 8. (a) Box plots of GB velocity values v_t for abnormal GBs, grouped by low-angle (misorientation angle $\overline{\varphi}_t \leq 15°$) and high-angle GBs ($\overline{\varphi}_t > 15°$), with the number of GBs in each box plot indicated by the blue number. Bivariate kernel density estimates of mean velocity values $\overline{v}_{\mathrm{con},t}$ of abnormal GBs connected to (b) low-angle and (c) high-angle abnormal GBs with velocity v_t. The bisector line (dashed blue line) denotes equality of the values of $\overline{v}_{\mathrm{con},t}$ and v_t. The measured values of $(v_t, \overline{v}_{\mathrm{con},t})$ are plotted as red dots.

6. Discussion

A reliable quantification of GB migration behavior requires GBs to undergo a minimum measurable displacement. Small GB velocity values v_t may arise from discretization errors in the image data, inaccuracies in image registration, or deviations in fitted surface representations. Given an image resolution of 1.78 µm and a time interval of 15 min between successive grain mappings, a three-voxel displacement corresponds to a velocity of 0.356 µm min^{-1}. Consequently, abnormal GBs serve as optimal subjects for studying migration behavior, as their velocity values, at least on average, exceed the detectable threshold. Utilizing this robust population of GBs, we now address two relevant aspects of GB mobility: first, the extent to which abnormal migration aligns with conventional curvature-driven growth models, and second, the kinematic constraints and dynamic interactions imposed by neighboring boundaries interconnected via triple junctions.

6.1. **Curvature-driven grain growth**

As evident in Figure 5, abnormal GBs undergoing sufficiently large displacement migrate toward their center of curvature, as the values of the mean displacement angles remain consistently below the 90° threshold for anticurvature behavior. However, there is no monotonic—in particular, no linear—relationship between GB velocity and mean curvature values observable, as indicated by an SCC value of 0.013 and the visual impression given by Figure 4(c). This finding is consistent with recent studies of GB migration in Ni, $SrTiO_3$ and Fe polycrystals [10, 14, 47]. Overall, no clear dependency of GB velocity on mean curvature is observed, indicating that curvature is not the primary driving force for migration in this material, or possibly that such a dependency may be observable only in conjunction with additional GB characteristics. The absence of a correlation between the GB velocity and the mean curvature might result from a number of aspects of grain growth, including the topological constraints imposed by neighboring GBs, the anisotropy of GB properties, or the buildup of internal stresses associated with shear-coupled GB migration [13].

Further insight into the behavior of fast abnormal GBs can be gleaned from Figure 9, which visualizes the migration of three GBs during a 15-min annealing period. In Figures 9(a), (b) and (c), each GB is illustrated as a triangular mesh, with the face color-coded based on the local mean curvature value H_t (linearly interpolated from the vertices). The sign of each H_t value is determined such that the local normal vector at each respective point is directed toward the reader. The values of H_t present at the triple junctions are treated as outliers and are therefore excluded from the migration analysis. As detailed in Section 3, GB migration is quantified by establishing a pointwise correspondence between surface representations over two consecutive time steps. Figures 9(d), (e) and (f) illustrate the resulting displacement vectors, which are color-coded by their corresponding velocity values $v_{\mathrm{loc},t}$. The arrows correspond to the displacement vectors of GB points located at least 3.56 µm (2 voxels) away from triple junctions. The GBs exhibit mean displacement angles $\overline{\alpha}_t$ around 21°, 77° and 9°, GB velocities v_t of 1.35, 0.01 and 0.89 µm min^{-1}, mean curvatures $\overline{H}_t$ of 0.018, 0.027 and 0.021 $\mu\mathrm{m}^{-1}$ and mean influences $\overline{\lambda}_{h,t}$ of 0, 0.005 and 0.006, respectively. Thus, the morphological evolution and migration kinetics of the examined GBs present several distinct behaviors. For the first GB, shown in Figures 9(a) and (d), the upper-left segment exhibits the most pronounced displacement, yet its local mean curvature does not vary significantly from that of less mobile regions, such as the segment on the right. Furthermore, point tracking is absent in the upper-left region of the GB; the migration of the adjoining triple junction induces localized shrinkage and annihilation of the GB area in this section. However, for the second GB in Figures 9(b) and (e), the boundary features the highest mean curvature among all three GBs but the lowest velocity. Similarly to the first GB, its upper-left region undergoes the most extensive displacement, while its lower-right segment migrates away from its center of curvature. In contrast, the third GB shown in Figures 9(c) and (f) migrates entirely toward its center of curvature, similar to the behavior of the first GB. However, the third GB undergoes significant morphological alterations along its lower section. This is because a neighboring GB exhibits a strong movement there, causing a large displacement of the triple junction shared with the third GB. Notably, the third GB's resulting alteration is not captured by the velocity tracking framework, since GB migration is only considered for points that can be tracked, i.e., for which a displacement vector can be computed. Despite the localized lack of correlation between GB velocity and mean curvature, on the whole, the fast GBs in the first and third rows of Figure 9 exhibit migration toward their respective center of curvature, as evidenced by the small mean displacement angles.

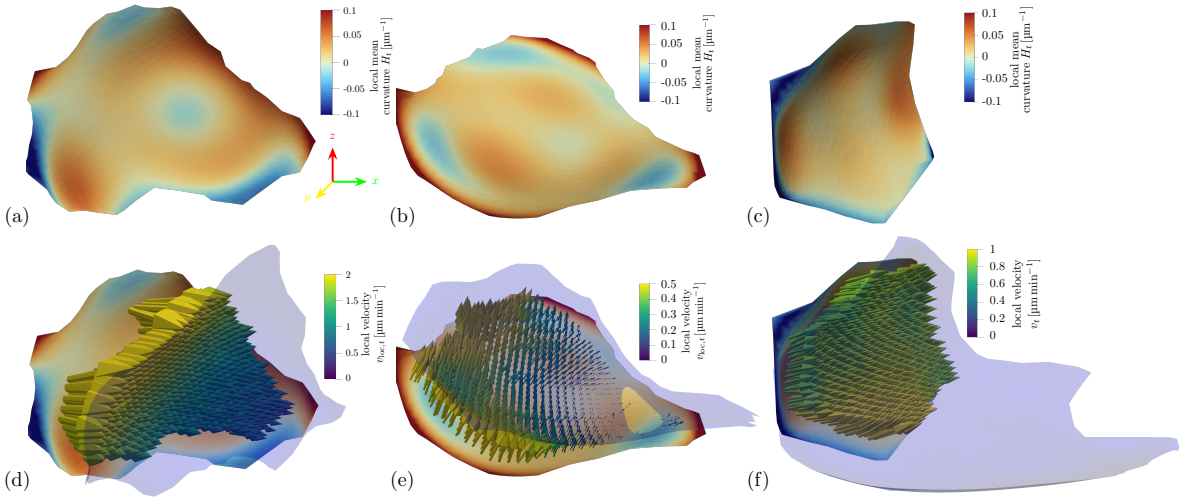


FIGURE 9. Visualization of morphology (a,b,c) and evolution (d,e,f) of three GBs as triangular mesh plots. The triangular surfaces are colored according to the linearly interpolated values of local mean curvature H_t at the vertices of the triangles, and the arrows—colored according to the values of local GB velocity—represent the displacement at each GB point.

6.2. **Influence of GB connectivity**

As illustrated in Figure 9(f), GB migration is potentially constrained or driven by network dynamics as the lower section of the GB exhibits a strong movement, which results from the movement of a GB connected by a triple junction. This demonstrates that the GB network topology could exert an important influence on migration rates together with local morphological features like mean curvature. This network effect, quantified in Section 5.2.2, reveals a high correlation between velocities of adjacent boundaries. Notably, low-angle GBs act as structural constraints within the network: their consistently low mobility exerts a localized pinning effect, retarding the migration kinetics of connected neighboring GBs (Figure 7(b)), which in turn causes all connected boundaries to exhibit low velocity values on average, too. In Table 1, values of mean curvature, GB velocity and velocity of connected GBs are shown for four low-angle GBs that were observable over all time steps. These low-angle GBs are of particular interest, as they exhibit increasing mean curvature values over time as only regions close to its triple junction migrate. Thus, for these GBs the conventional curvature-driven grain growth model cannot hold. Furthermore, GBs connected to these low-angle GBs exhibit relatively low velocity values on average—in particular, at later time steps, when grains from the high-angle GBs connected to these low-angle GBs may already have been consumed by the abnormally growing grain. Overall, these low-angle GBs lead to the impression that GB velocity is not linearly correlated with mean curvature, at least for these types of abnormal GBs. Thus, our findings suggest that neglecting network effects is a potential inherent limitation of curvature-based GB migration equations [2, 3], and thus these models could be improved by incorporating the influence of interconnected GB networks on individual GB behavior, instead of treating each GB as an isolated object.

TABLE 1. Values of mean curvature $\overline{H}_t$, GB velocity v_t and neighboring GB velocity $\overline{v}_{\mathrm{con},t}$ of low-angle GBs with corresponding misorientation angle $\overline{\varphi}_t$ at the time steps of $t = 15, 30, 45, 60$ and 75 min.

$\overline{\varphi}_t$ [°]	$\overline{H}_t$ [µm^{-1}]					v_t [µm min^{-1}]					$\overline{v}_{\mathrm{con},t}$ [µm min^{-1}]				
	15	30	45	60	75	15	30	45	60	75	15	30	45	60	75
7.98	0.019	0.03	0.03	0.034	0.042	0.067	0.11	0.095	0.049	0.096	0.42	0.074	0.064	0.111	0.055
9.98	0.014	0.03	0.031	0.032	0.029	0.047	0.072	0.062	0.095	0.096	0.415	0.291	0.358	0.062	0.078
11.05	0.027	0.037	0.036	0.037	0.035	0.095	0.11	0.078	0.056	0.095	0.632	0.636	0.172	0.064	0.097
14.98	0.014	0.012	0.014	0.022	0.021	0.094	0.079	0.089	0.195	0.085	0.291	0.071	0.304	0.481	0.06

7. Conclusions

In this study, we have extended the analysis of GB migration dynamics during AGG presented in [26] by systematically investigating the interplay between GB morphology, migration velocity and the potential pinning effect of second-phase particles. To this end, we modified the method proposed in [30], representing GBs extracted from image data as continuous surfaces using spherical harmonics. This enables us to approximate GBs with higher accuracy, particularly at triple junctions, and represent strongly curved GBs associated with island grains or grains with peninsula-shaped boundaries, see Appendix A. The representation of the latter GB types is particularly important, since the fast migration of abnormal GBs into the surrounding matrix typically leads to the formation of peninsulas, which is why such boundary morphologies must be represented accurately in a comparison of abnormal to matrix-matrix GB behavior. Our findings advance the fundamental understanding of GB kinetics beyond conventional curvature-driven migration models by demonstrating that, although the local GB migration velocity is not correlated with the mean curvature, the local boundary morphology significantly determines the direction of displacement of fast migrating GBs. Abnormal GBs are significantly more curved than matrix-matrix GBs, for which almost no migration was observed, supporting the curvature-driven migration model. Our investigation of the influence of second-phase particles on GB migration behavior—in particular, through the introduction of descriptors for the local influence of these particles on GB migration—provides no evidence to support the hypothesis that abnormal grains preferentially grow into regions with below-average particle density. Furthermore, the connectivity of the GB network exerts an important influence on GB migration behavior. The results suggest that low-angle GBs exhibit a localized pinning effect, slowing the migration of connected neighboring GBs. To better understand the migration dynamics governed by GB networks, future research could employ numerical simulations to model and analyze topological constraints, potentially leading to more accurate prediction of microstructure evolution in polycrystalline materials.

Data availability statement

The datasets generated and/or analyzed during the current study are available from the corresponding author on reasonable request.

Conflicts of interest statement

The authors declare that they have no conflict of interest, and the funding agencies played no role in the design of the study; in the collection, analysis or interpretation of data; in the writing of the manuscript; or in the decision to publish the results.

Author contributions

Conceptualization, **V. Schmidt**, **C.E. Krill III**; data curation, **H.-A. Schulz-Harder**, **J.M. Dake**; formal analysis, **T. Wilhelm**; funding acquisition, **V. Schmidt**, **C.E. Krill III**; investigation, **T. Wilhelm**; methodology, **T. Wilhelm**, **O. Furat**, **H.-A. Schulz-Harder**, **J.M. Dake**; project administration, **V. Schmidt**, **C.E. Krill III**; resources, **T. Wilhelm**, **H.-A. Schulz-Harder**, **J.M. Dake**; software, **T. Wilhelm**, **H.-A. Schulz-Harder**, **J.M. Dake**; supervision, **V. Schmidt**, **C.E. Krill III**; visualization, **T. Wilhelm**, **H.-A. Schulz-Harder**; writing – original draft, **T. Wilhelm**; writing – review & editing, **T. Wilhelm**, **H.-A. Schulz-Harder**, **O. Furat**, **J.M. Dake**, **V. Schmidt**, **C.E. Krill III**;
All authors have read and agreed to the published version of the manuscript.

Acknowledgments

This research is partially funded by the German Research Foundation (DFG) under project number 453092613 (KR 1658/9-1, SCHM 997/41-1) and by the Federal Ministry of Research, Technology and Space (BMFTR) under project number 05K26VUA.

References

[1] T. Sutoki. On the mechanism of crystal growth by annealing. *Science Reports of the Tohoku Imperial University*, 17:857–876, 1928.

[2] J. Burke and D. Turnbull. Recrystallization and grain growth. *Progress in Metal Physics*, 3:220–292, 1952.

[3] M. Hillert. On the theory of normal and abnormal grain growth. *Acta Metallurgica*, 13: 227–238, 1965.

[4] B. L. Adams and T. Olson. The mesostructure—properties linkage in polycrystals. *Progress in Materials Science*, 43:1–87, 1998.

[5] M. A. Groeber, B. K. Haley, M. D. Uchic, D. M. Dimiduk and S. Ghosh. 3D reconstruction and characterization of polycrystalline microstructures using a FIB–SEM system. *Materials Characterization*, 57:259–273, 2006.

[6] D. J. Rowenhorst, A. C. Lewis and G. Spanos. Three-dimensional analysis of grain topology and interface curvature in a β-titanium alloy. *Acta Materialia*, 58:5511–5519, 2010.

[7] H. F. Poulsen. *Three-Dimensional X-Ray Diffraction Microscopy: Mapping Polycrystals and Their Dynamics*. Springer, 2004.

[8] M. McKenna, S. O. Poulsen, E. M. Lauridsen, W. Ludwig and P. W. Voorhees. Grain growth in four dimensions: A comparison between simulation and experiment. *Acta Materialia*, 78:125–134, 2014.

[9] A. Bhattacharya, Y. F. Shen, C. M. Hefferan, S. F. Li, J. Lind, R. M. Suterm and G. S. Rohrer. Three-dimensional observations of grain volume changes during annealing of polycrystalline Ni. *Acta Materialia*, 167:40–50, 2019.

[10] Z. Xu, Y. Shen, S. K. Naghibzadeh, X. Peng, V. Muralikrishnan, S. Maddali, D. Menasche, A. R. Krause, K. Dayal, R. M. Suter and G. S. Rohrer. Grain boundary migration in polycrystalline α-Fe. *Acta Materialia*, 264:119541, 2024.

[11] Z. Xu, J. Sun, J. M. Dake, J. Oddershede, H. Kaur, S. K. Naghibzadeh, C. E. Krill III, K. Dayal and G. S. Rohrer. Grain boundary properties and microstructure evolution in an Al-Cu alloy. *Acta Materialia*, 292:121041, 2025.

[12] G. B. Bizana and L. A. Barrales-Mora. Kinetics of grain boundary migration in nanosized Al polycrystals. *Acta Materialia*, 260:1359–6454, 2023.

[13] C. Qiu, D. J. Srolovitz, G. S. Rohrer, J. Han and M. Salvalaglio. Why grain growth is not curvature flow. *Proceedings of the National Academy of Sciences*, 122:e2500707122, 2025.

[14] V. Muralikrishnan, H. Liu, L. Yang, B. Conry, C. J. Marvel, M. P. Harmer, G. S. Rohrer, M. R. Tonks, R. M. Suter, C. E. Krill III and A. R. Krause. Observations of unexpected grain boundary migration in $SrTiO_3$. *Scripta Materialia*, 222:115055, 2023.

[15] L. Yang, V. Muralikrishnan, V. Yadav, Z. Tian, J. B. Harley, A. R. Krause and M. R. Tonks. Beyond curvature-driven grain growth: Insights from fully anisotropic Monte Carlo Potts simulations. *Acta Materialia*, 302:121672, 2026.

[16] C. E. Krill III, E. A. Holm, J. M. Dake, R. Cohn, K. Holíková and F. Andorfer. Extreme abnormal grain growth: connecting mechanisms to microstructural outcomes. *Annual Review of Materials Research*, 53:319–345, 2023.

[17] A. Rollett. Abnormal grain growth and texture development. *Materials Science Forum*, 495-497:1171–1176, 2005.

[18] H.-C. Kim, C.-G. Kang, M.-Y. Huh and O. Engler. Effect of primary recrystallization texture on abnormal grain growth in an aluminum alloy. *Scripta Materialia*, 57:325–327, 2007.

[19] J. Humphreys, G. S. Rohrer and A. Rollett. *Recrystallization and Related Annealing Phenomena*. Elsevier, 3rd edition, 2017.

[20] W. T. Read and W. Shockley. Dislocation models of crystal grain boundaries. *Physical Review*, 78:275–289, 1950.

[21] F. J. Humphreys. A unified theory of recovery, recrystallization and grain growth, based on the stability and growth of cellular microstructures—I. The basic model. *Acta Materialia*, 45:4231–4240, 1997.

[22] C. S. Smith. Grains, phases and interfaces–an interpretation of microstructure. *American Institute of Mining and Metallurgical Engineers*, 175:15–51, 1948.

[23] T. Gladman. On the theory of the effect of precipitate particles on grain growth in metals. *Proceedings of the Royal Society of London. Series A, Mathematical and Physical Sciences*, 294:298–309, 1966.

[24] J. Dennis, P. S. Bate and F. J. Humphreys. Abnormal grain growth in Al–3.5Cu. *Acta Materialia*, 57:4539–4547, 2009.

[25] M. Wang. *Reverse Engineering the Kinetics of Grain Growth in Al-based Polycrystals by Microstructural Mapping in 4D*. Phd thesis, Ulm, University, 2022.

[26] H.-A. Schulz-Harder, K. Gutbrod, M. Atzen, M. Ziehmer, T. Wilhelm, O. Furat, H. Fang, O.-P. Autran, W. Ludwig, M. Bernacki, V. Schmidt, C. E. Krill III and J. M. Dake. Tracking the emergence and persistence of abnormal grain growth in an aluminum alloy using diffraction-contrast tomography. *arXiv preprint arXiv:2610.31176*, 2026.

[27] W. Ludwig, P. Reischig, A. King, M. Herbig, E. M. Lauridsen, G. Johnson, T. J. Marrow and J. Y. Buffière. Three-dimensional grain mapping by X-ray diffraction contrast

tomography and the use of friedel pairs in diffraction data analysis. *Review of Scientific Instruments*, 80:033905, 2009.

[28] J. Zhang, Y. Zhang, W. Ludwig, D. Rowenhorst, P. W. Voorhees and H. F. Poulsen. Three-dimensional grain growth in pure iron. Part I. Statistics on the grain level. *Acta Materialia*, 156:76–85, 2018.

[29] B. Zoofan, J.-Y. Kim, S. I. Rokhlin and G. S. Frankel. Phase-contrast x-ray imaging for nondestructive evaluation of materials. *Journal of Applied Physics*, 100:014502, 2006.

[30] T. Wilhelm, O. Furat, J. M. Dake, C. E. Krill III and V. Schmidt. A computational framework for tracking grain boundaries in 3D image data: Quantifying boundary curvatures and velocities in polycrystalline materials. *Computational Materials Science*, 267:114541, 2026.

[31] J. M. Dake, J. Oddershede, H. D. Sørensen, T. Werz, J. C. Shatto, K. Uesugi, S. Schmidt and C. E. Krill III. Direct observation of grain rotations during coarsening of a semisolid Al–Cu alloy. *Proceedings of the National Academy of Sciences*, 113:E5998–E6006, 2016.

[32] J. Dake. *Experimental Investigations of Microstructural Coarsening in 3D using X-Ray Microscopy*. Phd thesis, Ulm University, 2020.

[33] S. Beucher and F. Meyer. The morphological approach to segmentation: The watershed transformation. In E. R. Dougherty, editor, *Mathematical Morphology in Image Processing*, pages 600–612. Marcel Dekker Inc., 1993.

[34] P. Soille. *Morphological Image Analysis: Principles and Applications*. Springer, 2013.

[35] C. R. Maurer, R. Qi and V. Raghavan. A linear time algorithm for computing exact euclidean distance transforms of binary images in arbitrary dimensions. *Analysis and Machine Intelligence*, 25:265—270, 2003.

[36] J. Feinauer, A. Spettl, S. Manke, S. Strege, A. Kwade, A. Pott and V. Schmidt. Structural characterization of particle systems using spherical harmonics. *Materials Characterization*, 106:123—133, 2015.

[37] B. Prifling, D. Westhoff, D. Schmidt, H. Markötter, I. Manke, V. Knoblauch and V. Schmidt. Parametric microstructure modeling of compressed cathode materials for li-ion batteries. *Computational Materials Science*, 169:109083, 2019.

[38] O. Furat, L. Petrich, D. P. Finegan, D. Diercks, F. Usseglio-Viretta, K. Smith and V. Schmidt. Artificial generation of representative single li-ion electrode particle architectures from microscopy data. *npj Computational Materials*, 7:105, 2021.

[39] P. Gräfensteiner, E. Löwer, O. Furat, U. A. Peuker and V. Schmidt. Artificial filter cake generation: Digital twins via stochastic 3D modeling based on µ-CT image data. *Powder Technology*, 452:120550, 2025.

[40] A. Kelemen, G. Székely and G. Gerig. Elastic model-based segmentation of 3-D neuroradiological data sets. *IEEE Transactions on Medical Imaging*, 18:828–839, 2002.

[41] P. Gräfensteiner, J. Friebel, L. Ditscherlein, O. Furat, U. A. Peuker and V. Schmidt. An AFM-based approach for quantification of guest particle deformation during mechanofusion. *Powder Technology*, 434:119293, 2024.

[42] H. Edelsbrunner, D. G. Kirkpatrick and R. Seidel. On the shape of a set of points in the plane. *IEEE Transactions on Information Theory*, 29:551–559, 1983.

[43] N. Akkiraju, H. Edelsbrunner, M. Facello, P. Fu, E. P. Mucke and C. Varela. Alpha shapes: Definition and software. In *Proceedings of the 1st International Computational Geometry Software Workshop*, pages 63–66, 1995.

[44] G. Leobacher and F. Pillichshammer. *Introduction to Quasi-Monte Carlo Integration and Applications*. Springer, 2014.

[45] V. Randle and O. Engler. *Introduction to Texture Analysis: Macrotexture, Microtexture and Orientation Mapping*. CRC Press, 2000.

[46] M. Wang, S. Wu and C. E. Krill III. Extraction of grain boundary curvature from voxel-based representations of polycrystalline microstructures. *IOP Conference Series: Materials Science and Engineering*, 580:012048, 2019.

[47] A. Bhattacharya, Y. Shen, C. M. Hefferan, S. F. Li, J. Lind, R. M. Suter, C. E. Krill III and G. S. Rohrer. Grain boundary velocity and curvature are not correlated in Ni polycrystals. *Science*, 374:189–193, 2021.

[48] V. A. Epanechnikov. Non-parametric estimation of a multivariate probability density. *Theory of Probability and its Applications*, 14:153–158, 1987.

[49] C. Spearman. The proof and measurement of association between two things. *The American Journal of Psychology*, 15:72–101, 1904.

[50] J. K. Mackenzie. Second paper on statistics associated with the random disorientation of cubes. *Biometrika*, 45:229–240, 1958.

[51] D. W. Scott. *Multivariate Density Estimation: Theory, Practice, and Visualization*. J. Wiley & Sons, 2015.

[52] Z. Fan, Y. Wu, X. Zhao and Y. Lu. Simulation of polycrystalline structure with Voronoi diagram in Laguerre geometry based on random closed packing of spheres. *Computational Materials Science*, 29:301–308, 2004.

[53] A. Lyckegaard, E. M. Lauridsen, W. Ludwig, R. W. Fonda and H. F. Poulsen. On the use of Laguerre tessellations for representations of 3D grain structures. *Advanced Engineering Materials*, 13:165–170, 2011.

[54] A. Spettl, T. Brereton, Q. Duan, T. Werz, C. E. Krill III, D. P. Kroese and V. Schmidt. Fitting Laguerre tessellation approximations to tomographic image data. *Philosophical Magazine*, 96:166–189, 2016.

[55] O. Šedivý, J. M. Dake, C. E. Krill III and V. Schmidt. Description of the 3D morphology of grain boundaries in aluminium alloys using tessellation models generated by ellipsoids. *Image Analysis & Setreology*, 36:5–13, 2017.

[56] O. Šedivý, D. Westhoff, J. Kopeček, C. E. Krill III and V. Schmidt. Data-driven selection of tessellation models describing polycrystalline microstructures. *Journal of Statistical Physics*, 172:1223–1246, 2018.

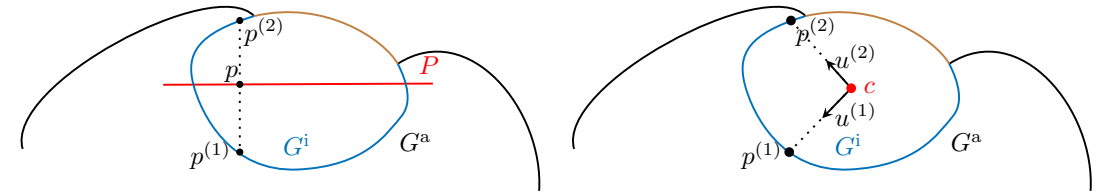
[57] R. Quey and L. Renversade. Optimal polyhedral description of 3D polycrystals: Method and application to statistical and synchrotron X-ray diffraction data. *Computer Methods in Applied Mechanics and Engineering*, 330:308–333, 2018.

[58] L. Petrich, O. Furat, M. Wang, C. E. Krill III and V. Schmidt. Efficient fitting of 3D tessellations to curved polycrystalline grain boundaries. *Frontiers in Materials*, 8:760602, 2021.

Appendix

A. Validation of the surface representation method based on spherical harmonics

In this study, we modified the methodology introduced in [30] for constructing surface representations based on smoothing thin-plate splines by employing spherical harmonics instead. This alternative approach enables the representation of GBs associated with peninsula-shaped grains. Such GBs begin to curve back on themselves, a phenomenon that occurs in particular during abnormal grain growth, and for such GBs the method introduced in [30] remains applicable only locally. More precisely, the method proposed in [30] requires the surface S constructed by a surface function $s : K \to \mathbb{R}$ to be a function that maps a point $(p_x, p_y) \in K$ for a set $K \subset \mathbb{R}^2$ to a unique value $p_z = s(p_x, p_y) \in \mathbb{R}$, such that the point (p_x, p_y, p_z) is located on the surface representation S; see Figure 10(a) for the case of a schematic peninsula-shaped GB. For two GB points $p^{(1)} \in B$ and $p^{(2)} \in B$ on the GB B (blue line) between the island grain G^{i} and a grain G^{a}, their orthogonal projection onto the plane $P \subset \mathbb{R}^3$ leads to the same point $p \in P$. Thus, it is not possible to construct a function $s\colon P \to B$ representing B. By contrast, the use of spherical harmonics allows the entire GB of such grains to be represented as a surface in Figure 10(b), where the GB is represented using spherical harmonics utilizing the center c (red dot) of the island grain as the star point and direction vectors $u^{(1)}$ and $u^{(2)}$ of two GB points $p^{(1)}$ and $p^{(2)}$. This is achieved by selecting a star point and defining direction vectors from this point to each GB point. Consequently, the method proposed in this paper not only accommodates a broader class of GB geometries but also yields a conceptually simpler surface representation. In particular, unlike the thin-plate spline–based approach, it does not require additional preprocessing steps for each GB prior to surface fitting.



(a) (b)

FIGURE 10. 2D illustration of the challenges associated with the surface representation of the GB B of an island grain G^{i} and an abnormal grain G^{a} with GB points $p^{(1)}$ and $p^{(2)}$ (black dots) using (a) the thin-plate spline interpolation approach with projection plane P (red line) and (b) the spherical harmonics–based surface representation methodology with star point c (red dot) and direction vectors $u^{(1)}$ and $u^{(2)}$ between c and $p^{(1)}$ and $p^{(2)}$, respectively.

Furthermore, the spherical harmonics-based approach provides improved accuracy in the representation of GBs, particularly in regions near triple junctions. To evaluate the accuracy of the proposed method and compare it to the thin-plate spline-based approach, we applied the same procedure as in [30] using distance-based tessellation models [52–58], which partition a given volume of three-dimensional Euclidean space into distinct regions that parametrically represent the individual grains of a polycrystal. Tessellation models have been found to exhibit GB structures comparable to those observed in real microstructures and have been previously fitted to experimental data [55, 56, 58]. In particular, a multiplicatively weighted Laguerre tessellation has been utilized in [30], where the interface of two neighboring tessellation cells,

which in this context is related to a GB, is analytically defined by a quadratic surface. This analytic representation allows for a direct comparison between the analytic GB and the fitted surface representation with respect to local mean curvature values. We evaluate the capability of the model to represent GBs by the local accuracy of the mean curvature computation. Therefore, we use the relative error $\varepsilon_{\mathrm{rel}} \in [0, \infty)$ between the analytic local mean curvature values and the values obtained with the proposed surface representation based on spherical harmonics (see Section 4.1). In addition, during model validation, we take into account the Euclidean distance between the GB points and triple junctions. The lower accuracy of the proposed surface representation methods near triple junctions is expected, owing to the reduced number of points available for surface fitting. Therefore, we evaluated the models with respect to the surface representations given by Eq. (10) for various values of $d_{\mathrm{min}} \geq 0$, restricting the evaluation of the model accuracy to points that are located at least a distance d_{min} from the triple junctions.

Figure 11 presents box plots of the relative error $\varepsilon_{\mathrm{rel},d_{\mathrm{min}}}$ across various values of d_{min}, comparing thin-plate splines (red) and spherical harmonics (black) for surface representation. The median and mean values of each box plot are indicated by brown and orange lines, respectively, while the blue curve shows the number of GBs considered by the analysis at each d_{min} value. As d_{min} increases, points on smaller GBs are successively excluded from the analysis until all points are excluded, thus reducing the total sample size available for model validation. The spherical harmonics-based approach consistently yields lower $\varepsilon_{\mathrm{rel},d_{\mathrm{min}}}$ values than the thin-plate spline method, as evidenced by lower mean and median values across all d_{min} configurations. However, both methods exhibit elevated values of $\varepsilon_{\mathrm{rel},d_{\mathrm{min}}}$ at lower values of the threshold d_{min}, which can be attributed to the inherent sensitivity of mean-curvature computations to second-order numerical derivatives. Consequently, minor discrepancies between the fitted surface and the analytical GB can induce substantial relative errors in the estimated local mean curvature. This indicates that a robust evaluation of curvature requires the exclusion of GB points in close proximity to triple junctions for both methods. Consistent with the benchmarks reported in [30], the surface representation based on spherical harmonics demonstrates superior accuracy relative to the thin-plate spline-based representation.

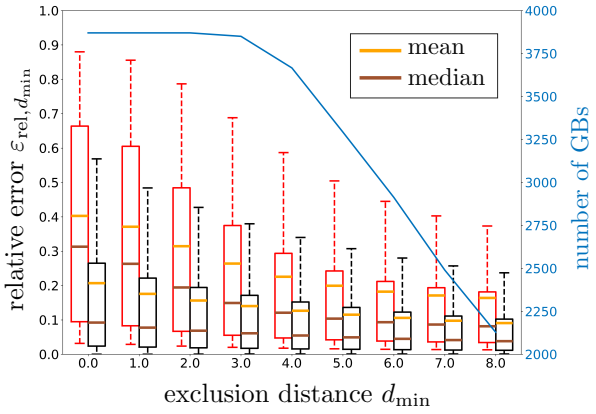


FIGURE 11. Relative errors $\varepsilon_{\mathrm{rel}}$ of computed mean curvature values H_t and their ground truth values using thin-plate splines (red boxes) and spherical harmonics (black boxes) for the surface representation method, excluding all points with distance less than d_{min} from triple junctions. The number of GBs that remain after application of the d_{min} criterion is indicated by the blue curve.

B. Velocity of vanishing GBs

In this section, we provide additional details regarding the velocity approximation of vanishing GBs. In the literature [46, 47], the velocity of a GB between two adjacent grains is often approximated by the ratio of the exchanged volume of these grains and the average interfacial area between the same grain pair, normalized by time—i.e., the GB velocity is approximated by

$$\widetilde{v}_{\mathrm{ex}} = \frac{V_{\mathrm{ex}}}{\frac{1}{2}(A_t + A_{t+\Delta t})\Delta t}, \tag{19}$$

where V_{ex} denotes the exchanged volume and $A_t, A_{t+\Delta t}$ the surface areas at time steps t and $t + \Delta t$, respectively. However, in the case of vanishing GBs it is not possible to determine the surface area $A_{t+\Delta t}$ and, thus we modify the formula given in Eq. (19) to account for vanishing GBs.